STUDYING ELECTROOSMOSIS OF VISCOPLASTIC CASSON FLUID USING LATTICE-POISSON-BOLTZMANN METHOD

S. Derakhshan* **M. Rezaee** **H. Sarrafha**

School of Mechanical Engineering
Iran University of Science & Technology
Tehran, Iran

ABSTRACT

A numerical investigation of an electroosmotic flow through a microchannel is presented. Lattice Poisson-Boltzmann method was utilized to determine the effective geometrical and electrokinetic parameters in a microfluidic system. The non-Newtonian fluid model is assumed to be viscoplastic which is suitable for modeling biologic structures. These types of fluids are shown to have a yield stress which affects the velocity profile significantly. Unlike Casson fluid constitutive properties, electrokinetic parameters are shown not to be effective on the yielded region in the microchannel. The influence of flow and viscokinetic parameters on yield height, plug-flow velocity and mass flow rate was studied and discussed.

Keywords: Casson fluid, Electroosmosis, Lattice blotzmann method, Numerical analysis.

1. INTRODUCTION

Micro-Electro-Mechanical devices (MEMs) are among the most interesting fields in recent technological advances. These devices are utilized in many applications including biomechanics, medicine, microelectronics cooling devices, and space explorations. Among MEMs various devices, micropumps are probably the most famous and frequently utilized ones. They are used for pumping or manipulating very small volumes of fluids [1].

Since the first micropumps were introduced in the early 1980s, a very rapid progress has been in place in micropumps development and analysis. In a very general categorization, micropumps are split into two catagories: displacement (mechanical) and dynamic (non-mechanical) [1]. In displacement micropumps, different mechanisms based on motion of the components are used to pump the flow. On the contrary, there exist no moving components in dynamic micropumps, instead the electrochemical reaction between the fluid and the channel walls causes continuous fluid pumping. Therefore, only certain types of fluids with specific properties are possible to be pumped using this mechanism [1].

Most of the recent efforts in this field are about displacement micropumps [1] and among displacement micropumps most of the studies investigate piezoelectrically driven displacement micropumps. The number of reported efforts on dynamic micropumps is much lower than displacement micropumps and among dynamic micropumps, electrohydrodynamic, magnetohydrodynamic, and electroosmotic micropumping are the most popular, respectively [1, 2]. Each of dynamic micropump mechanisms is appropriate for a specific application depending on the fluid, the environment, the applicable power source and etc. [1]. Recent researches are almost completely devoted to different types of dynamic micropumps. Among dynamic micropumps, electroosmotic type is probably the most popular and specifically appropriate for medical and bio-fluids applications.

When an electrolyte solution contacts a solid surface with specific characteristics, a local ionization could take place at the fluid-solid interface such that a very thin layer of ions (in the scale of nanometers) forms within the fluid near the wall, which is called the electric double layer (EDL). The thickness of the EDL is calculated $\kappa^{-1} = [\varepsilon k_B T/(2e^2 z^2 n_\infty)]$ in which κ^{-1} that is called the debye length represents a measure of the EDL thickness, $\varepsilon = \varepsilon_r \varepsilon_0$ represents the electrical permittivity of the solution (ε_r represents the dielectric constant of the solution and ε_0 represents the electrical permittivity of vacuum), k_B represents the Boltzmann constant, T represents the solution absolute temperature, e represents the charge of an electron, z represents the valence of the ions of the solution, and $n_\infty = c_\infty N_A$ represents the bulk ionic number of the solution (c_∞ is bulk ionic concentration of the solution and N_A is the Avogadro's number). This local ionization produces a local electric potential φ that if exposed to an external electric field E, a bulk fluid mo-

* Corresponding author (shderakhshan@iust.ac.ir)

DOI : 10.1017/jmech.2017.33
Copyright © 2017 The Society of Theoretical and Applied Mechanics
https://doi.org/10.1017/jmech.2017.33 Published online by Cambridge University Press

tion is observed. This is due to the appliance of coulomb forces as $f_{Coulomb} = \rho_E E$, in which ρ_E represents the charge density distribution near the walls, and consequently, the friction force between fluid layers. The velocity of this flow depends on both the construction material of the walls and the solution parameters [3]. This phenomenon is called electroosmosis, in which the electric potential is only formed near the walls and the bulk fluid potential as well as charge density is zero [3].

EO flow is used in a wide range of applications, including soil remediation, and has been used in chemical and biological analysis since at least 1974 [1]. The flow rates produced by the most basic EO pumps are typically very small (Q_{max} < 1 μl min^{-1}). Most of the studies about EO micropumps before 2005 are dedicated to fabrication and experimental studies [1], while in recent years most of the studies focus on numerical as well as analytical investigations, since these types of study are simpler while providing useful information especially for very small scale micropumps, experimental test of which is yet impractical. Beside studies involving molecular dynamics [4, 5], here the works done by utilizing microscale methods are of interest [6]. Wang *et al*. numerically investigated the electroosmotic flow of Newtonian fluids in microchannels using lattice-Poisson-Boltzmann method [7]. They showed that in an electrically driven osmotic flow field, the flow velocity increases with both external electrical field intensity and surface zeta potential for a homogeneous channel flow [7]. Boyd *et al*. analyzed the Casson and Carreau-Yasuda non-Newtonian blood models in steady and oscillatory flows using the lattice Boltzmann method [8]. Their attempt is among the pioneer attempts performed about electroosmotic flow of non-Newtonian fluid fl ows. Berli and Olivares studied the electrokinetic flow of non-Newtonian fluids in microchannels theoretically [9]. Yoshino *et al*. presented a numerical method for incompressible non-Newtonian fluid flows based on the lattice Boltzmann method in 2007 [10]. Also, Tang *et al*. this flow numerically in 2008 [11]. Zhao and Yang presented an analytical relation for Nonlinear Smoluchowski velocity for electroosmosis of Power-law fluids over a surface with arbitrary zeta potentials [12]. Berli reported theoretical expressions of the flow rate, output pressure and thermodynamic efficiency of electrokinetic pumping of non-Newtonian fluids through cylindrical and slit microchannels in 2009 [13]. Vasu and De analytically studied the Electroosmotic flow of power-law fluids at high zeta potentials in 2010 [14]. Hadigol *et al*. numerically analyzed the mixed electroosmotic/pressure driven flow of power-law fluids in microchannels and micropumps in 2010 [15]. They showed that increase in zeta potential or decrease in EDL thickness results in larger pressure rises and volumetric flow rates of EO micropumping of pseudo-plastic fluids, while these changes do not have considerable effects on pressure rise and the volumetric flow rate of EO micropumping of dilatant fluids [14]. Also, Nosrati *et al*. investigated the effect of y-component electroosmotic body force in mixed electroosmotic/pressure driven microflows [16]. In another attempt, Hadigol *et al*. studied the electroosmotic micromixing of non-Newtonian fluids numerically [17]. Zhao and Yang presented an exact solution for electroosmosis of non-Newtonian fluids in microchannels [18]. Chiu-On Ng studied the combined pressure driven electroosmotic flow of Casson fluid through a slit microchannel analytically in 2013 [19]. It is showed that even a small value of the Casson yield stress can considerably reduce the rate of flow of the fluid through a microchannel by electroosmosis. Zhao and Yang published a comprehensive review on the performed studies about electrokinetics of non-Newtonian fluids [19]. Also, Yang and Yong performed an asymptotic analysis on the lattice Boltzmann method for generalized Newtonian fluid flows [20]. Chiu-On Ng and Qi presented analytical relations for Electroosmotic flow of a viscoplastic material through a slit channel with walls of arbitrary zeta potential [21]. It is shown in the study that materials of different models will exhibit qualitatively different asymptotic behaviors [21]. Their attempt is among the latest performed studies about electroosmotic flow of viscoplastic fluid flows. Finally, Derakhshan *et al*. numerically studied electroosmotic micropump performance using Lattice Boltzmann method [22].

As discussed, most of the applications using EO micropumps somehow involve non-Newtonian fluids due to the solution requirements for such a mechanism [23]. In spite of some useful analytical solutions of Casson fluid which has been presented in the literature [19], effects of parameters such as Casson constant are not studied as far as the authors know. The interest here lies in investigating this type of flow from a numerical prospect. Furthermore, it would be interesting to examine the validation of simplifying assumptions of the analytical solution using the numerical method. Therefore it is attempted to study the electroosmotic flow of viscoplastic Casson fluids by the numerical approach. In the next section, the theoretical and numerical framework of the investigated problem is illustrated. In section 3 the simulation results are presented, described, and discussed. And in the final section, the conclusions deduced from the results are summarized.

2. THEORETICAL AND NUMERICAL FRAMEWORK

2.1 Rheological Behavior of Casson Fluid

The fluid studied in this paper is assumed to be viscoplastic, i.e. it has a yield stress. Some of the common models include Bingham, Casson, and Eyring models. The fluid domain in these fluids is divided into two yielded and unyielded regions. The portion of the fluid within which the shear stress exceeds the yield stress is called the yielded region and the other portion of the fluid is called the unyielded region. The height at which the two flow regions separate is called the yield height. Viscoplastic fluids possess a two-equation constitutive model and therefore, their constitutive equation is not continuous and a smoothed version of the constitu-

https://doi.org/10.1017/jmech.2017.33 Published online by Cambridge University Press

tive model shall be used in numerical simulations. The Casson fluid model is assumed in this study, since some of the important non-Newtonian bio-fluids are modeled using Casson model and acceptable results are acquired. The constitutive equation of the Casson fluid proposed by Casson is formulated as follows [19, 24]:

$$\eta_P \dot{\gamma} = \begin{cases} [1-\sqrt{\tau_0 / |\tau|}]^2 & \text{for } |\tau| > \tau_0, \\ 0 & \text{for } |\tau| \le \tau_0 \end{cases} \quad (1)$$

where τ is the shear stress tensor, $\dot{\gamma} = (\nabla \boldsymbol{u}) + (\nabla \boldsymbol{u})^T$ is the rate of deformation tensor ($\boldsymbol{u}$ is the velocity vector), η_P is the plastic viscosity, $\tau_0 \ge 0$ is the Casson yield stress and

$$|\tau| = \sqrt{\frac{1}{2}\tau : \tau}, \quad (2)$$

is the magnitude of the stress. In [25], the smoothed version of the Casson model is as follows [20]:

$$\mu(\dot{\gamma}) = \left[\sqrt{\frac{\tau_0}{\tau}} (1 - e^{-\sqrt{m\dot{\gamma}}}) + \sqrt{\eta_P} \right]^2 \quad (3)$$

in which μ is the dynamic viscosity and m is the regularization parameter. The yield stress value of human blood (as an example) is between 0.01 and 0.06 dyn/cm^2.

2.2 Governing Equations

In this study, time-independent flow of dilute non-Newtonian electrolyte solution with Casson model as the constitutive equation is considered through a two-dimensional slit microchannel. Also, the flow is assumed to be purely electroosmotic. The system is in chemical equilibrium state and the transport process is steady. It is assumed that the ions in the near-wall region are absorbed to the slid surface rigidly and they have no contribution to bulk ion movement. The average velocity is low, hence the convection effects are neglected. Also, the bulk ion concentration is not very high or very low so that the Poisson-Boltzmann (PB) equation can be used [26, 27]. Due to negligible convection effects and moderate ion concentration, the ion transport can be described using a weak-coupling Poisson–Boltzmann model instead of the strong-coupling Poisson–Nernst–Plank model [27]. For a univalent solution, the equations describing the electrokinetic transport are expressed as follows [3, 27, 28]:

$$\nabla^2 \varphi = \frac{2en_\infty}{\varepsilon_r \varepsilon_0} \sinh\left(\frac{e\varphi}{kT}\right) \quad (4)$$

$$\rho_e = -2en_\infty \sinh\left(\frac{e\varphi}{kT}\right) \quad (5)$$

which are the governing equations for electric potential and

$$\nabla . \boldsymbol{u} = 0 \quad (6)$$

$$\rho \boldsymbol{u} . \nabla \boldsymbol{u} = -\nabla p + \mu \nabla^2 \boldsymbol{u} + \rho_e \boldsymbol{E} \quad (7)$$

which are the evolution equations for hydrodynamics.

2.3 Formulation of Lattice Poisson Blotzman Method (LPBM) for Non-Newtonian Microscale Fluid

The Boltzmann transport equation for a system with an external force can be written as follows [29]:

$$\frac{\partial f}{\partial t} + c.\nabla f + \frac{F}{m}\frac{\partial f}{\partial c} = \Omega \quad (8)$$

in which $f(r, c, t)$ is the distribution function, which is defined as the probability of finding particles within a certain range of velocities at a certain range of locations at a given time, c is the particle speed, r is the particle location, m is the particle mass, F is the external force, and Ω(f) is the collision operator, which is the function determining the particle density variation due to particle collisions [29]. The relation between the above equation and macroscopic quantities such as fluid density, ρ, and fluid velocity vector, $\boldsymbol{u}$, is as follows:

$$\rho(\boldsymbol{r}, t) = \int m f(\boldsymbol{r}, \boldsymbol{c}, t) d\boldsymbol{c} \quad (9)$$

$$\rho(\boldsymbol{r}, t)\boldsymbol{u}(\boldsymbol{r}, t) = \int m \boldsymbol{c} f(\boldsymbol{r}, \boldsymbol{c}, t) d\boldsymbol{c} \quad (10)$$

Assuming the BGK collision operator the Boltzmann transport equation can be written as [29]:

$$\frac{\partial f_i}{\partial t} + c_i \nabla f_i + \frac{F}{m}\frac{\partial f_i}{\partial c_i} = \frac{1}{\tau}(f_i^{eq} - f_i) \quad (11)$$

in which the subscript i represents the lattice ith direction, τ is the dimensionless relaxation time and f_i^{eq} is the Maxwell-Boltzmann distribution function defined as follows [29]:

$$f(c) = \left(\frac{m}{2\pi k_B T}\right)^{3/2} e^{-\frac{mc^2}{2k_B T}} \quad (12)$$

If we discretize the solution domain to certain number of lattices each point having a distribution function, equation (11) can be discretized to:

$$f_i(\boldsymbol{r} + \boldsymbol{c}_i \delta_t, t + \delta_t) - f_i(\boldsymbol{r}, t) = -\frac{1}{\tau}[f_i(\boldsymbol{r}, t) - f_i^{eq}(\boldsymbol{r}, t)] + \delta_t F_i \quad (13)$$

in which δ_t is the time step and $\boldsymbol{c}_i$ is the discrete velocity. For the common D2Q9 lattice arrangement, the discrete velocity can be written as [29]:

$$\boldsymbol{c}_i = \begin{cases} (0,0) & i = 0 \\ (1,0)c, (0,1)c, (-1,0)c, (0,-1)c & i = 1,4 \\ (1,1)c, (-1,1)c, (-1,-1)c, (1,-1)c & i = 4,8 \end{cases} \quad (14)$$

in which $c = \delta_x/\delta_t$ represents the lattice speed (δ_x is the lattice size). Also, the relaxation time is defined as [27]:

$$\tau = 0.5 + 3\nu / \delta_x c \quad (15)$$

https://doi.org/10.1017/jmech.2017.33 Published online by Cambridge University Press

in which v is the kinematic viscosity. The equilibrium distribution function can be expressed as [27]:

$$f_i^{eq} = \omega_i \rho \left[1 + 3\frac{\boldsymbol{c}_i.\boldsymbol{u}}{c^2} + 9\frac{(\boldsymbol{c}_i.\boldsymbol{u})^2}{2c^2} - \frac{3u^2}{2c^2} \right] \tag{16}$$

while the weight functions are defined as [7]:

$$\omega_i = \begin{cases} 4/9 & i = 0 \\ 1/9 & i = 1,4 \\ 1/36 & i = 4,8 \end{cases} \tag{17}$$

The external force term can be discretized [27]:

$$F_i = \frac{3\rho_e \boldsymbol{E}.(\boldsymbol{c}_i - \boldsymbol{u})}{\rho c^2} f_i^{eq} \tag{18}$$

and the fluid density and velocity can be calculated as [27, 29]:

$$\rho = \sum_i f_i \tag{19}$$

$$\rho \boldsymbol{u} = \sum_i \boldsymbol{c}_i f_i \tag{20}$$

It could be shown that equations (13-20) turn into the described governing equations using Chapman-Enskog analysis [29].

In the studies about simulation of Newtonian fluid electroosmosis, parameter τ is taken to be constant throughout the simulation process [22]. However, in this study τ is shear-dependent at each node, because the viscosities of non-Newtonian fluids vary with the shear rate [27]. For Casson fluids, the correlation between kinematic viscosity and shear strain tensor can be stated as follows:

$$\begin{aligned} \nu &= \left[\sqrt{\frac{\tau_0}{\dot{\gamma}} \left(1 - e^{-\sqrt{m\dot{\gamma}}} \right)} + \sqrt{\eta_P} \right]^2 \Big/ \rho \\ &= \left[\sqrt{\frac{\tau_0}{\tau} \left(1 - e^{-\sqrt{m(S_{\alpha\beta}S_{\alpha\beta})}} \right)} + \sqrt{\eta_P} \right]^2 \Big/ \rho \end{aligned} \tag{21}$$

Artoli [30] derived the formula for calculating the shear strain tensor using non-equilibrium distribution function:

$$S_{\alpha\beta} = -\frac{3}{2\rho c^2 \tau} \sum_i f_i^{(1)} c_{i\alpha} c_{i\beta} \tag{22}$$

where $f_i^{(1)}$ is the first order term of the non-equilibrium distribution function [22]. Since high order (≥ 2) terms are infinitesimals compared to the first order term, we approximately consider the whole non- equilibrium distribution function as the first order non-equilibrium distribution function [27]

$$f_i^{(1)} \approx f_i^{neq} = f_i - f_i^{eq} \tag{23}$$

Combining Eqs. (21-23) and (15), one can derive a shear-dependent relaxation time τ with density distribution functions at each node. This procedure enables us to incorporate the Casson constitutive model into the LPBM numerical method.

Analogously, the same discrete evolution equation could be produced for electric potential distribution. Note that unlike the discrete evolution equation of particle distribution functions (known as LBM), the evolution equation of electric potential distribution does not have physical interpretation and it is simply a mathematical trick using analogy in order to solve the non-linear Poisson-Boltzmann equation (known as LPM). If we combine equations (4) and (5), the non-linear Poisson-Boltzmann equation for the general charge density solution is acquired by [7]:

$$\nabla^2 \varphi = -\frac{1}{\varepsilon} \sum_i z_i e n_{i,\infty} \exp\left(-\frac{z_i e}{k_B T} \varphi \right) \tag{24}$$

Where subscript i represents the ith species and z is the valence of the ions (including the sign). The solution of equation (24) can be considered as the steady solution of the equation [7]:

$$\frac{\partial \varphi}{\partial t} = \nabla^2 \varphi + g_{rhs}(\boldsymbol{r}, \varphi, t), \tag{25}$$

where

$$g_{rhs} = \frac{1}{\varepsilon} \sum_i z_i e n_{i,\infty} \exp\left(-\frac{z_i e}{k_B T} \varphi \right) \tag{26}$$

represents the negative right hand side (RHS) term in the original Poisson equation [7].

Hence, the evolution equation for the electrical potential on two-dimensional discrete lattices can be written as [7, 27]:

$$\begin{aligned} &g_i(\boldsymbol{r} + c_i \delta_{t,g}, t + \delta_{t,g}) - g_i(\boldsymbol{r}, t) \\ &= -\frac{1}{\tau_g} [g_i(\boldsymbol{r}, t) - g_i^{eq}(\boldsymbol{r}, t)] + \left(1 - \frac{0.5}{\tau_g} \right) \delta_{t,g} \omega_i g_{rhs} \end{aligned} \tag{27}$$

with the equilibrium distribution of g:

$$g_i^{eq} = \bar{\omega}_i \varphi \tag{28}$$

with

$$\bar{\omega}_i = \begin{cases} 0, & i = 0, \\ 1/6 & i = 1,2,3,4, \\ 1/12 & i = 5,6,7,8. \end{cases} \tag{29}$$

The time step in equation (27) is [7]:

$$\delta_{t,g} = \frac{\delta_x}{\acute{c}} \tag{30}$$

where $\acute{c}$ is pseudo speed of sound in the potential field. In fact it can be artificial to change the time step [7]. The dimensionless relaxation time for Eq. (27) is

$$\tau_g = \frac{3\chi \delta_{t,g}}{2\delta_x^2} + 0.5 \tag{31}$$

https://doi.org/10.1017/jmech.2017.33 Published online by Cambridge University Press

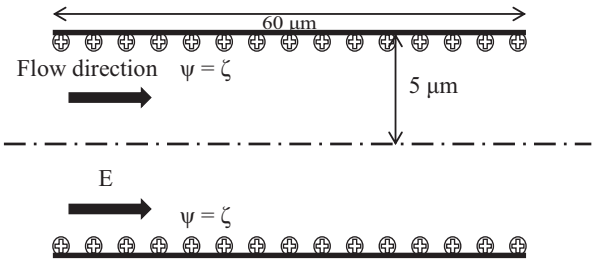


Fig. 1 Geometry of the system.

where χ, which is equal to unity in the simulations, is defined as the potential diffusivity [7].

The equations (27)-(31) are consistent with the Poisson equation (25) [7]. After evolving on the discrete lattices, the macroscopic electrical potential can be calculated by:

$$\varphi = \sum_i (g_i + 0.5\delta_{t,g} g_{rhs} \omega_i). \tag{32}$$

Although the electrical potential evolution equations are of unsteady nature, only the steady state result is realistic [7].

2.4 Geometry and Grid Specifications

The defined geometry of the problem is depicted in Fig. 1. As it is seen from the figure, the electroosmotic flow within a 2D rectangle with uniform zeta potential on the walls is analyzed. The width and length of the rectangle are assumed to be 60 μm and 10 μm, respectively. The flow domain is meshed with a uniform grid. Every cell is a square with length of h = 40 nm. Also, a D2Q9 lattice model is considered and the time step is taken to h^2, due to stability reasons. Also, the fluid electrical permittivity is assumed to be 690×10^{-12} F/m always in this study.

2.5 Boundary Conditions

For the hydrodynamic (LBM) equations, the non-equilibrium bounce-back rule should be applied to the north and south boundaries [27, 31]. In order to do so, it can be considered that

$$f_\alpha^{neq} = f_\beta^{neq} \tag{33}$$

Where the subscripts α and β represent the opposite directions [22]. For the east and west boundaries fully developed flow boundary condition is considered for the hydrodynamic equations and the distribution functions of f_1, f_5, and f_8 are assumed to have the same values for the first two lattice columns for the west boundary condition and the distribution functions of f_6, f_3, and f_7 are assumed to have the same values for the last two lattice columns for the east boundary condition in order to do so.

For the LPM boundary conditions, Dirichlet boundary condition was used for the electrical potential on the wall surfaces and the Neumann condition was used at the inlet and outlet sections [3].

For the Dirichlet boundary, the unknown distribution functions were calculated from the local equilibrium distribution with the source, g_{rhs} [7, 32]. For example, for the upper wall, g_4, g_7 and g_8 are unknown, but they can be obtained using the equilibrium distribution of local φ_0 [7]:

$$\varphi_0 = 3\zeta - 3S_P - 1.5\delta_t \sum_i \omega_i g_{rhs} \tag{34}$$

where S_P is the sum of known populations coming from the internal nodes and nearest wall nodes [7]:

$$S_P = g_0 + g_1 + g_2 + g_3 + g_5 + g_6. \tag{35}$$

Hence the unknown distributions are [7]:

$$g_i = \bar{\omega}_i \varphi_0 \tag{36}$$

The corner can be treated in a similar way, with five unknowns. The upper-right corner, for example, has the unknown populations g_3, g_4, g_5, g_7 and g_8 [7]. They also follow from Eq. (34) with [7]:

$$\varphi_0 = \frac{12\zeta - 6\delta_t \Sigma_i \omega_i g_{rhs} - 12 S_P}{7} \tag{37}$$

where:

$$S_P = g_0 + g_1 + g_2 + g_6. \tag{38}$$

The east and west boundary conditions for LPM was implemented the Neumann boundary conditions [7]. At the east boundary (the left section, for example), the relation:

$$\varphi_0 = 3S_P + 1.5\delta_t \sum_i \left(\frac{g_{rhs} \omega_i c_{i,x}}{c} \right) \tag{39}$$

with:

$$S_P = g_1 + g_5 + g_8 \tag{40}$$

can be applied to determine the unknown populations g_3, g_6 and g_7 [7].

3. SIMULATION RESULTS AND DISCUSSION

3.1 Grid Independency and Validation

The validity of the modeling system for Casson fluid was investigated by comparing the numerical obtained velocity profile to those of the analytical solutions in the literature [19]. To this regard, the simplest case was considered where $\alpha, \beta = 0$ and $\kappa = 100$. Figure 2 shows that there is acceptable coincidence between the two sets of results.

To investigate the grid independency of the results, the averasge velocity across half of the channel width is estimated using different fining grids and the acquired results are plotted in Fig. 3. As it is seen from the figure, the average velocity shows a sudden variation at about 101 lattices along the channel width but after that

https://doi.org/10.1017/jmech.2017.33 Published online by Cambridge University Press

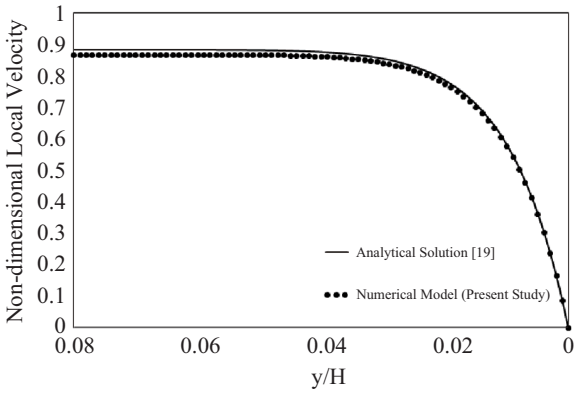


Fig. 2 Validation of present simulation model by comparison of obtained velocity profile, for the case of $\beta = 0$, $\kappa = 100$ and $\alpha = 0$.

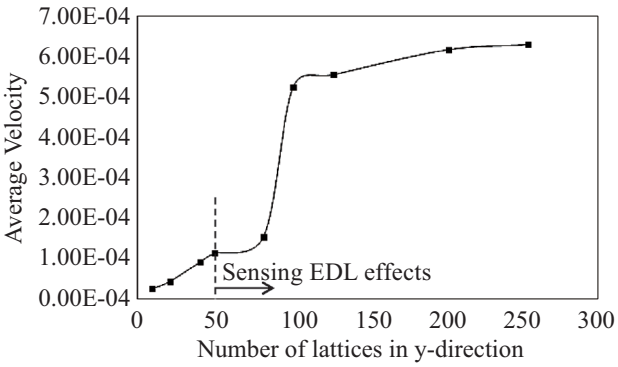


Fig. 3 Grid independency of the results, average velocity plotted for different grid sizes.

Table 1 Percentage variation versus grid cell size

Grid cell size (nm)	Average velocity (m/s)	Variation percentage
1000	2.865444E-5	-
500	4.513128E-5	57.50%
250	8.971934E-5	98.80%
200	1.132861E-4	26.27%
125	1.478747E-4	30.53%
100	5.283282E-4	257.28%
80	5.532656E-4	4.72%
50	6.123837E-4	10.68%
40	6.311890E-4	3.07%

smoothly varies and is approximately constant for number of lattices more than 201. For this diagram κH = 200. Therefore, the EDL thickness approximately equals 50 nm and the significant difference at about number of lattices 101 is because the solution senses the EDL effect gradually as the grid becomes finer. Table 1 shows the error percentage for different number of lattices. The gird size is assumed to be 40 nm in this study.

3.2 Knudsen Number Investigation

As in every micro-scale analysis, there is a limit here for grid refinement beyond which the inter-molecular forces are significant and the solution domain is no longer continuous. Knudsen number defined as $Kn = \lambda/l$, in which λ represents molecular mean free path of the fluid and l represents the characteristic length of the flow, determines this limit so as for $Kn < 0.01$ the flow domain is assumed to be continuous, for $Kn \approx 1$ the flow is assumed to be within the transient region, and for $Kn > 100$ molecular dynamics governs the flow behavior. Lattice Boltzmann equations are derived considering the continuous flow regime equations. Therefore, the grid size as the characteristic length of the flow must satisfy this condition. For water we have

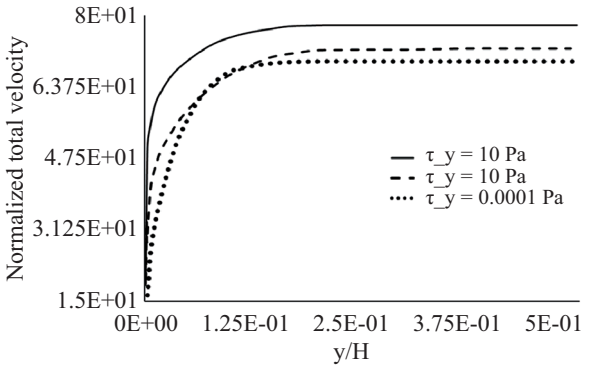


Fig. 4 Normalized total velocity versus non-dimensional channel height for different Casson yield stresses.

$$\lambda = \frac{1}{n\sigma} \tag{41}$$

where $n = N_A / M_{H_2O}$ is the water molecules number density, $M_{H_2O} = 18$ is the molecular mass of water, N_A is the Avogadro's number, and $\sigma = \pi r^2$, in which r is the water molecule's radius. Therefore, after some calculation it is revealed that for $Kn < 0.01$ condition to hold, the grid size may not be smaller than 25 nm. As we have aqueous solutions in our problem, it could be claimed that for grid sizes larger than 25 nm, the flow is continuous and the lattice Boltzmann formulation is applicable.

3.3 Velocity Profile Investigation

The velocity profile and its determining parameters are investigated in this section. Figure 4 shows the normalized total velocity versus non-dimensional channel height for different Casson yield stresses at E = 1000V, ξ = 15 mV, κH = 100, and Casson constant = 1. It should be noted that the velocities are normalized by Smoluchowski velocity for Newtonian fluids [17], which is calculated as follows:

$$u_s = \tau_E / \mu\kappa = -\epsilon\xi E / \mu \tag{42}$$

https://doi.org/10.1017/jmech.2017.33 Published online by Cambridge University Press

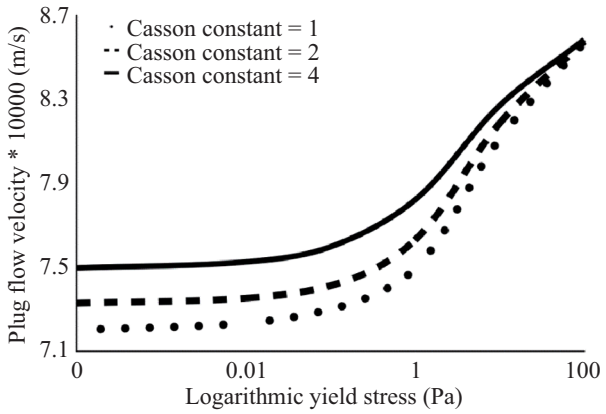


Fig. 5 Multiplied plug-flow velocity versus logarithmic yield stress for different Casson constants.

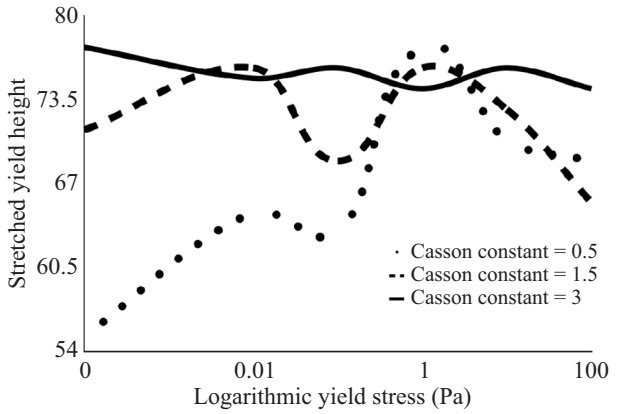


Fig. 6 Variation of the stretched yield height versus the Logarithmic yield stress.

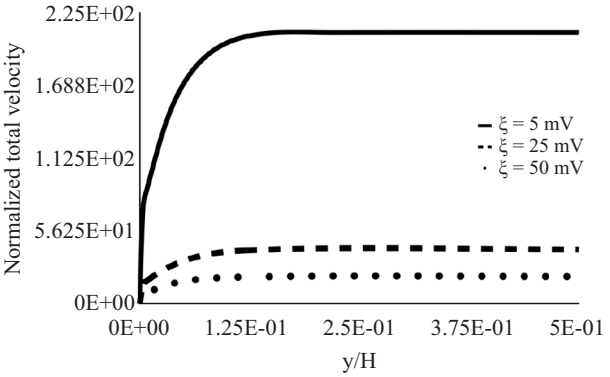


Fig. 7 Normalized total velocity profile across the channel for different zeta potentials at E = 1000V.

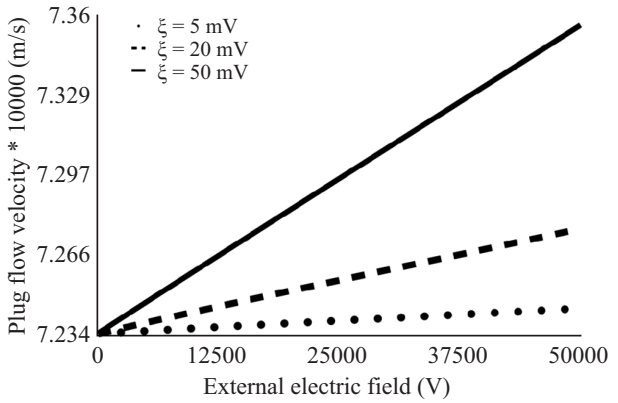


Fig. 8 Multiplied plug-flow velocity variation with the external electric field for different zeta potentials.

Generally, the velocity profile is plug-like within the microchannel, as seen in Fig. 4. It is seen that as the yield stress is increased the domain under velocity gradient becomes smaller, which is obvious since for higher yield stresses, the wall shear stress gets closer to the yield stress and a larger area of the fluid remains unyielded. In other words, the yield height is larger for smaller yield stresses. Also, it is seen in Fig. 4 that the plug-flow velocity is increased as the yield stress is increased. Figure 5 shows the variation of plug-flow velocity with the logarithmic yield stress for different Casson constants at E = 1000 V, ξ = 20 mV, and κH = 100.

It is seen from Fig. 5 that as the yield stress is increased, the plug-flow velocity is also increased with approximately the same trend for different Casson constants. It is seen that at very large yield stresses, the plug-flow velocity for different Casson constants approximately gets the same, which equals the upper limit for the plug-flow velocity.

Also, Fig. 6 shows the variation of stretched yield height with the yield stress for different Casson constants. It is seen from the figure that, as the Casson constant is increased, the slope of the variation of the yield height with the yield stress is decreased, i.e. for large Casson constants increasing the yield stress does not apply significant effect on the yield height.

Figure 7 shows the velocity profile for different zeta potentials at E = 1000 V, κH = 100, τ_y = 0.01 Pa, and Casson constant = 1. As it is seen from the figure, increasing the zeta potential significantly increases the plug-flow velocity as well as the average velocity. However, it does not significantly affect the yield height. Also, Fig. 8 shows the plug-flow velocity variation with the external electric field for different zeta potentials at the same conditions as Fig. 7. It is seen from the figure that the plug-flow velocity linearly varies with the external electric field and as the zeta potential is increased, the linear variation slope is also increased.

Figure 9 shows the yield height variation with the yield stress for different zeta potentials at the same conditions of Fig. 7 and Fig. 8. As is seen from the figure, the yield height is increased with zeta potential; however, its variation trend with the yield stress is approximately the same for different zeta potentials.

Figure 10 shows the normalized total velocity profile for different electric fields at τ_y = 0.01 Pa, κH = 100, and ξ = 50 mV. It is seen from the figure that increasing the

https://doi.org/10.1017/jmech.2017.33 Published online by Cambridge University Press

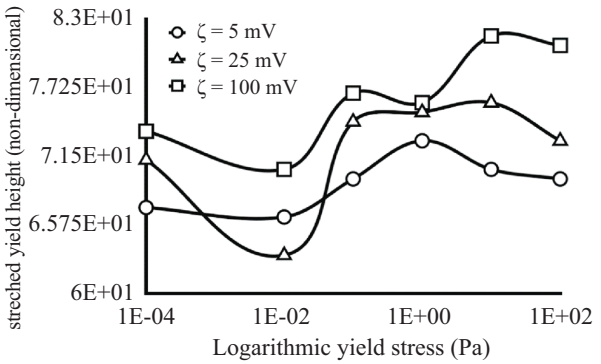


Fig. 9 Stretched yield height variation with Logarithmic yield stress for different zeta potentials.

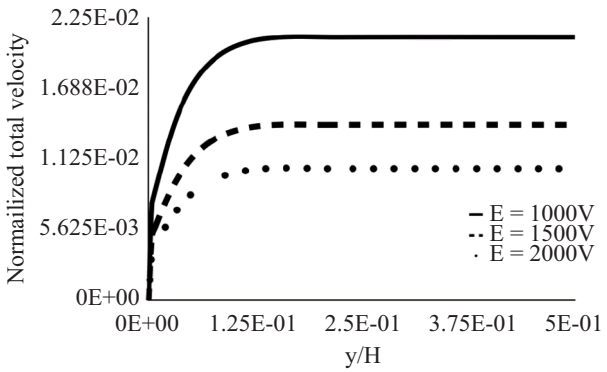


Fig. 10 Normalized total velocity profile for different electric field at constant zeta potential $\zeta = 50$ mV.

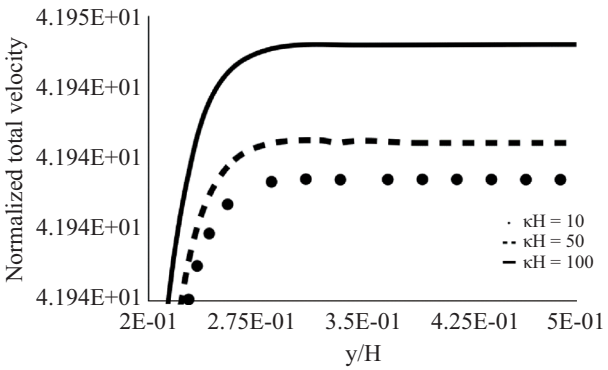


Fig. 11 Normalized total velocity profile for different electrokinetic parameters at constant electric field and zeta potential.

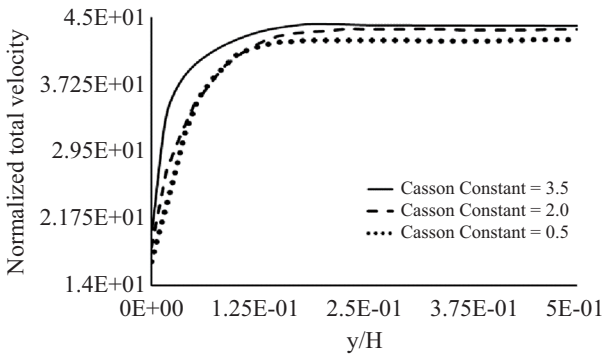


Fig. 12 Normalized total velocity profile for different Casson constants at constant electric field, zeta potential and yield stress.

electric field increases the average and plug-flow velocities, however, it does not affect the yield height. It is deduced that the electric field and zeta potential parameters apply the same effect on the average and plug-flow velocities. The important distinct between these results and those presented by the analytical solution [19] is that absolute total velocity is used here to show the velocity profile unlike the analytical solution where one dimensional velocity component is used.

Figure 11 shows the normalized total velocity profile for different electrokinetic parameters at E = 1000 V, $\xi = 25$ mV, $\tau_y = 0.01$ Pa, and Casson constant = 1. As it is seen from the figure, like other electric parameters (i.e. electric field and zeta potential), the electrokinetic parameter has no effect on the yield height and it affects the average and plug-flow velocity such that for larger electrokinetic parameters, the plug-flow and average velocities increase.

Figure 12 shows the normalized total velocity profile for different Casson constants at E = 1000 V, $\xi = 25$ mV, $\kappa H = 100$, and $\tau_y = 0.1$ Pa. It is seen from the figure that for different Casson constants, the velocity at the yield height stays the same. Also, the Casson constant does not affect the yield height; however, it slightly affects the plug-flow and average velocities. Moreover, it is observed that despite the constant yield velocity for

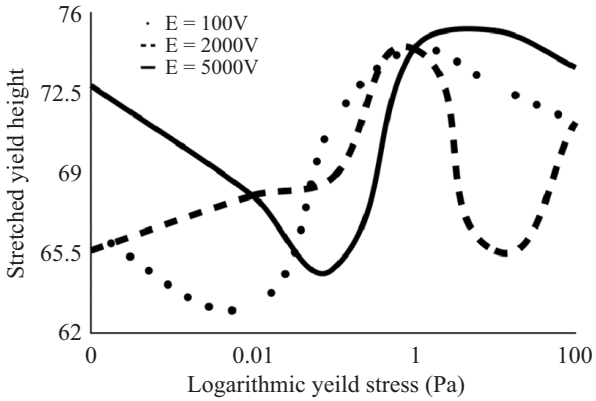


Fig. 13 Stretched yield height variation versus the logarithmic yield stress for different electric fields.

different Casson constants, the average velocity increases within the yield region as the Casson constant is increased.

Figure 13 depicts the yield height variation versus the yield stress for different electric fields at $\xi = 20$ mV, $\kappa H = 100$, and Casson constant = 1. It is seen from the figure that as the electric field is increased, the yield

https://doi.org/10.1017/jmech.2017.33 Published online by Cambridge University Press

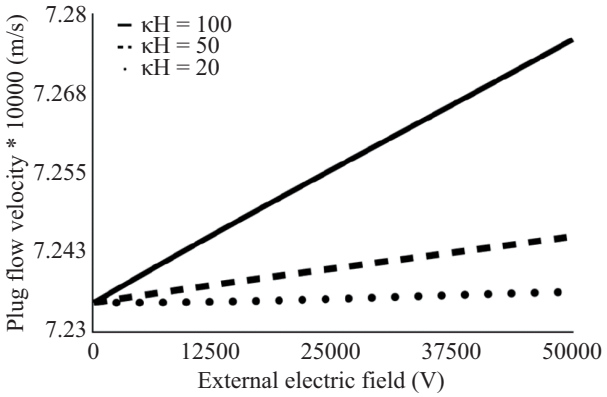


Fig. 14 Multiplied plug-flow velocity variation versus the external electric field for different electrokinetic parameters.

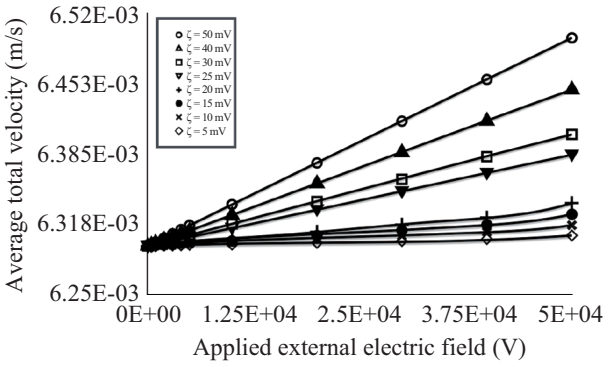


Fig. 15 Variation of average total velocity with respect to the applied external electric field variation for different zeta potentials.

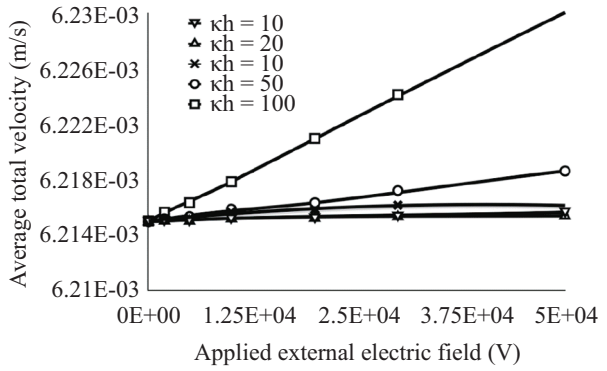


Fig. 16 Variation of average total velocity versus the applied external electric field for different electrokinetic parameters.

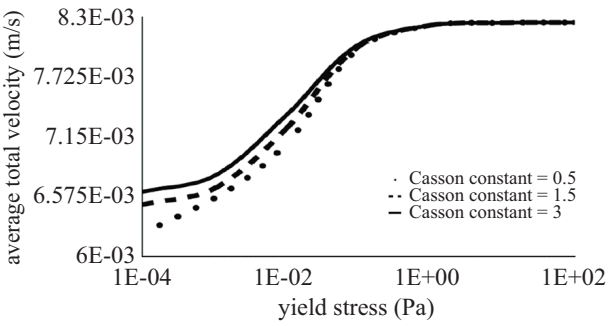


Fig. 17 Average velocity vs yield stress for different cases of Casson Constant.

height is generally increased. Also, Fig. 14 shows plug-flow velocity variation versus the external field for different electrokinetic parameters at ξ = 20 mV, τ_y = 0.01 Pa, and Casson constant = 1. It is observed like before that the plug-flow velocity has a linear relation with the external electric field and as the electrokinetic parameter is increased the variation line slope is also increased.

Figure 15 shows the average total velocity with respect to increasing applied external electric field for different zeta potentials at κH = 100, τ_y = 0.01 Pa, and Casson constant = 1. As it is shown in the figure, generally, the average total velocity increases with the external applied electric field. However, this increase is negligible for zeta potentials lower than 20 mV, but it is significant for zeta potentials higher than 25 mV. With a little investigation it is revealed that the boundary of these high and low zeta potential regions is specified by non-dimensional zeta potential of 1 (non-dimensional potential is calculated as $F\xi/RT$, where R is the universal gas constant), so that for non-dimensional zeta potentials lower than 1, the variation of average total velocity caused by the variation of the applied external electric field is negligible and for non-dimensional zeta potentials higher than 1, this variation is significant. Also, it is seen from the figure that the average total velocity varies linearly with the applied external electric field. Therefore, it could be deduced that at $\kappa H \gg 1$, which includes most of the cases, for $\hat{\xi} < 1$ increasing the applied external electric field does not significantly affect the total mass flow rate and therefore, it is not necessary and considering the providing costs, it may reduce the micropump efficiency. However, for $\hat{\xi} > 1$ this increase applies well effects on the micropump mass flow rate and therefore, its efficiency.

Figure 16 shows the variation of average total velocity versus the external electric field for different electrokinetic parameters at ξ = 25 mV, τ_y = 0.01 Pa, and Casson constant = 1. It is seen from the figure that like Fig. 16, the average total velocity and thereby the average mass flow rate is increased with the applied external electric field. Here again, as the electrokinetic parameter is increased, the slope of increasing line of the average total velocity is increased. However, it could be claimed that for electrokinetic parameters lower than κH = 30, increasing the external applied electric field applies negligible effect on the average total velocity and thereby, the average mass flow rate. Therefore, it could be claimed

https://doi.org/10.1017/jmech.2017.33 Published online by Cambridge University Press

that in such cases, lower external electric field can also provide the required mass flow rate and high external electric fields are not efficient.

Finally, Fig. 17 shows the average total velocity versus the Casson yield stress for different Casson constants. It is found that for yield stresses higher than τ_y = 0.1 Pa, the average total velocity is approximately the same for different Casson constants. However, for yield stresses τ_y < 0.1 Pa, for higher Casson constant the average total velocity is increase. Therefore, it could be deduced that while all other parameters are constant, for yield stresses lower than 0.1 Pa, fluid with higher Casson constants show higher average total velocity and thereby, higher mass flow rates.

4. CONCLUSIONS

In this study, the electroosmotic flow of Casson fluid through a slit microchannel was investigated via Lattice-Poisson-Boltzmann method. To this end a microchannel with 60 μm length and 10 μm height was considered and the flow was investigated through it. The Lattice-Poisson-Boltzmann was illustrated at first and its equations were presented. Then, the velocity profile, the plug-flow velocity, yield height, and the average flow velocity were investigated separately and various effective parameters on these were presented.

The electroosmotic flow within a microchannel shows a plug-like velocity profile. It was shown that parameters including the applied external electric field, the zeta potential, and the electrokinetic parameters do not affect the height at which the velocity profile is yielded, however, they affect the plug-flow velocity and therefore the average total velocity significantly. On the other hand, constitutive parameters such as Casson yield stress and Casson constant apply slight effects on the plug-flow velocity and average total velocity, however, they affect the yield height and the velocity profile within the yielded region near the wall, while keeping approximately the same behavior within the region far from the wall.

Also, it was deduced that at $\kappa H \gg 1$, which includes most of the cases, for $\hat{\xi} < 1$ increasing the applied external electric field does not significantly affect the total mass flow rate and therefore, it is not necessary and considering the providing costs, it may reduce the micropump efficiency. The same claim could be stated for the electrokinetic parameter as for electrokinetic parameters lower than κH = 30, increasing the external applied electric field applies negligible effect on the average total velocity and thereby, the average mass flow rate. Finally it could be deduced that while all other parameters are constant, for yield stresses lower than 0.1 Pa, fluid with higher Casson constants show higher average total velocity and thereby, higher mass flow rates. For future studies, other non-Newtonian viscoplastic Constitutive equations could be investigated and the results could be compared. Also, the study could be performed for smaller electrokinetic parameters, which requires slightly different governing equations, as the EDL effects are strengthened.

REFERENCES

1. Laser, D. J. and Juan G. S., "A Review of Micropumps," *Journal of Micromechanics and Microengineering*, **14**, pp. 35-64 (2004).
2. Si, D.-Q., Jian, Y.-J., Chang, L. and Liu, Q.-S., "Unsteady Rotating Electroosmotic Flow Through a Slit Microchannel," *Journal of Mechanics*, **32**, pp.1-9 (2016).
3. Kirby, B. J., *Micro- and Nanoscale Fluid Mechanics: Transport in Microfluidic Devices*, Cambridge University Press, London, England (2010).
4. White, C., Borg, M. K., Scanlon, T. J. and Reese, J. M., "A DSMC Investigation of Gas Flows in Micro-Channels with Bends," *Computers & Fluids*, **71**, pp. 261-271 (2013).
5. Derakhshan, S., Rezaee, M. and Sarrafha, H., "A Molecular Dynamics Study of Description Models for Shear Viscosity in Nanochannels: Mixtures and Effect of Temperature," *Nanoscale and Microscale Thermophysical Engineering*, **19**, pp. 206-220 (2015)
6. Derakhshan, S. and Yazdani, K., "3D Analysis of Magnetohydrodynamic (MHD) Micropump Performance Using Numerical Method," *Journal of Mechanics*, **32**, pp. 1-8 (2015).
7. Wang, J., Wang, M. and Li, Z., "Lattice-Poisson-Boltzmann Simulations of Electroosmotic Flows in Microchannels," *Journal of Colloid and Interface Science*, **296**, pp. 729-736 (2006).
8. Boyd, J., Buick, J. M. and Green, S., "Analysis of the Casson and Carreau-Yasuda Non-Newtonian Blood Models in Steady and Oscillatory Flows Using the Lattice Boltzmann Method," *Physics of Fluids (1994-present)*, **19**, 093103 (2007).
9. Berli, C. L. A. and Olivares, M. L., "Electrokinetic Flow of Non-Newtonian Fluids in Microchannels," *Journal of Colloid and Interface Science*, **320**, pp. 582-589 (2008).
10. Yoshino, M., Hotta, Y., Hirozane, T. and Endo, M., "A Numerical Method for Incompressible Non-Newtonian Fluid Flows Based on the Lattice Boltzmann Method," *Journal of non-Newtonian Fluid Mechanics*, **147**, pp. 69-78 (2007).
11. Tang, G. H., Li, X. F., He, Y. L. and Tao, W. Q., "Electroosmotic Flow of Non-Newtonian Fluid in Microchannels," *Journal of Non-Newtonian Fluid Mechanics*, **157**, pp. 133-137 (2009).
12. Zhao, C. and Yang, C., "Nonlinear Smoluchowski Velocity for Eectroosmosis of Power-Law Fluids over a Surface with Arbitrary Zeta Potentials," *Electrophoresis*, **31**, pp. 973-979 (2010).
13. Berli, C. L. A., "Output Pressure and Efficiency of

https://doi.org/10.1017/jmech.2017.33 Published online by Cambridge University Press

Electrokinetic Pumping of Non-Newtonian Fluids," *Microfluids and Nanofluids*, **8**, pp. 197-207 (2010).

14. Vasu, N., and De, S., "Electroosmotic Flow of Power-Law Fluids at High Zeta Potentials," *Colloids and Surfaces A: Physicochemical and Engineering Aspects*, **368**, pp. 44-52 (2010).
15. Hadigol, M., Nosrati, R. and Raisee, M., "Numerical Analysis of Mixed Electroosmotic/Pressure Driven Flow of Power-Law Fluids in Microchannels and Micropumps," *Colloids and Surfaces A: Physicochemical and Engineering Aspects*, **374**, pp. 142-153 (2011).
16. Nosrati, R., Hadigol, M. and Raisee, M., "The Effect of y-Component Electroosmotic Body Force in Mixed Electroosmotic/Pressure Driven Microflows," *Colloids and Surfaces A: Physicochemical and Engineering Aspects*, **372**, pp. 190-195 (2010).
17. Hadigol, M., Nosrati, R., Nourbakhsh, A. and Raisee, M., "Numerical Study of Electroosmotic Micromixing of Non-Newtonian Fluids," *Journal of non-Newtonian Fluid Mechanics*, **166**, pp. 965-971 (2011).
18. Zhao, C. and Yang, C., "An Exact Solution for Electroosmosis of Non-Newtonian Fluids in Microchannels," *Journal of Non-Newtonian Fluid Mechanics*, **166**, pp. 1076-1079 (2011).
19. Ng, C.-O., "Combined Pressure-Driven and Electroosmotic Flow of Casson Fluid Through a Slit Microchannel," *Journal of non-Newtonian Fluid Mechanics*, **198**, pp. 1-9 (2013).
20. Yang, Z. and Yong, W. A., "Asymptotic Analysis of the Lattice Boltzmann Method for Generalized Newtonian Fluid Flows," *Multiscale Modeling & Simulation*, **12**, pp. 1028-1045 (2014).
21. Ng, C.-O. and Qi, C., "Electroosmotic Flow of a Viscoplastic Material Through a Slit Channel with Walls of Arbitrary Zeta Potential," *Physics of Fluids*, **25**, 103102 (2013).
22. Derakhshan, S., Adibi, I. and Sarrafha, H., "Numerical Study of Electroosmotic Micropump Using Lattice Boltzmann Method," *Computers and Fluids*, **114**, pp. 232-241 (2015).
23. Kefayati, G. R., "Simulation of Vertical and Horizontal Magnetic Fields Effects on Non-Newtonian Power-Law Fluids in an Internal Flow Using FDLBM," *Computers and Fluids*, **114**, pp. 12-25 (2015).
24. Casson, N., "A Flow Equation for Pigment-Oil Suspensions of the Printing Ink Type," *Rheology of Disperse Systems,* Pergamon Press, London, pp. 84-104 (1959).
25. Neofytou, P. and Drikakis, D., "Non-Newtonian Flow Instability in a Channel with a Sudden Expansion", *Journal of Non-Newtonian Fluid Mechanics*, **111**, pp. 127-150 (2003).
26. Wang, M. and Chen, S. Y., "On Applicability of Poisson-Boltzmann Equation for Micro- and Nano-Scale Electroosmotic Flows," *Journal of Communications in Computational Physics*, **3**, pp. 1087-1099 (2008).
27. Chen, S., He, X., Bertola, V. and Wang, M., "Electro-Osmosis of Non-Newtonian Fluids in Porous Media Using Lattice Poisson–Boltzmann Method," *Colloid and Interface Science*, **436**, pp. 186-193 (2014).
28. Schoch, R. B., Han, J. and Renaud, P., "Transport Phenomena in Nanofluidics," *Reviews of Modern Physics*, **80**, 839 (2008).
29. Mohamad, A. A., *Lattice Boltzmann Method, Fundamentals and Engineering Applications with Computer Codes*, Springer-Verlag, London (2011).
30. Artoli, A. M., *Mesoscopic Computational Haemodynamics*, University of Amsterdam, Amesterdam (2003).
31. Zou, Q. and He, X., "On Pressure and Velocity Boundary Conditions for the Lattice Boltzmann BGK Model," *Physics of Fluids*, **9**, pp. 1591-1598, (1997).
32. D'Orazio, A. and Succi, S., "Simulating Two-Dimensional Thermal Channel Flows by Means of a Lattice Boltzmann Method with New Boundary Conditions," *Future Generation Computer Systems*, **20**, pp. 935-944 (2004).

(Manuscript received October 13, 2016,
accepted for publication May 1, 2017.)

https://doi.org/10.1017/jmech.2017.33 Published online by Cambridge University Press